# Experimental Investigation of Rotor Blade Structural Response In Hovering and Advance Flight at Low Reynolds Number Conditions

**Alexander D. Croke**
PhD Candidate
University of Glasgow
Glasgow, Scotland, UK

**Oliver D. Wild**
PhD Candidate
University of Maryland
College Park, Maryland, USA

**Anya R. Jones**
Professor
University of Maryland
College Park, Maryland, USA

**Richard B. Green**
Reader
University of Glasgow
Glasgow, Scotland, UK

## ABSTRACT

A towing tank investigation of a single rotor blade operating at hovering and high advance ratio conditions is presented. A custom blade was manufactured and instrumented with fully bridged axial strain gauges to monitor the flap bending strain at three radial locations. Measurements of rotor thrust and torque were obtained to characterise the rotor aerodynamic environment for advance ratios ranging from 0.4 to 1.00 and to identify the presence of stalled and reverse flow. Strain measurements obtained at three locations across the blade span show minima and maxima at approximately the same azimuthal location as the load data. Moreover, the strain distribution shows a growth in strain magnitude with increasing advance ratio. Spectra of strain shows a dominant 1/rev signal and for the $\theta = 25^o$ collective, non-harmonic frequencies are observed due to aperiodic vortex shedding from the presence of stalled flow.

## NOTATION

| | |
|---|---|
| A | Rotor disc area, $[m^2]$ |
| c | Blade chord, $[m]$ |
| $C_Q$ | Coefficient of torque, $Q/(\rho V_{tip}^2 AR)$, $[-]$ |
| $C_T$ | Coefficient of thrust, $T/(\rho V_{tip}^2 A)$, $[-]$ |
| D | Rotor disc diameter, $[m]$ |
| DOF | Degree of freedom |
| eVTOL | Electric vertical take-off and landing |
| $f$ | Frequency, $[Hz]$ |
| $\mathscr{F}(\cdot)$ | Fourier transform of function $\cdot$ |
| FB | Flap bending gauge |
| FoM | Figure of merit, $C_T^{3/2}/(C_Q\sqrt{2})$, $[-]$ |
| $(F_x,F_y,F_z)$ | Blade reference system |
| MAV | Micro air vehicle |
| NACA | National advisory committee for aeronautics |
| $N_b$ | Number of blades, $[-]$ |
| PIV | Particle image velocimetry |
| $Q$ | Rotor torque, $[Nm]$ |
| R | Rotor disc radius, $[m]$ |
| Re | Reynolds number, $[-]$ |
| $Re_{tip}$ | Rotor blade tip Reynolds number, $[-]$ |
| RPM | Revolutions per minute |
| RFDSV | Reverse flow dynamic stall vortex |
| STAL | Separated and transient aerodynamics laboratory |
| $T$ | Rotor thrust, $[N]$ |
| UAV | Unmanned air vehicle |
| $U_\infty$ | Freestream velocity, $[m/s]$ |
| $V_{tip}$ | Rotor blade tip velocity, $\Omega$R, $[m/s]$ |
| 2D/3D | Two/three dimensional |
| $\varepsilon_B$ | Bridge strain, $[-]$ |
| $\theta$ | Collective pitch angle, $[^\circ]$ |
| $\mu$ | Advance ratio, $U_\infty/(\Omega R)$, $[-]$ |
| $\nu$ | Kinematic viscosity, $[m^2/s]$ |
| $\rho$ | Fluid density, $[kg/m^3]$ |
| $\sigma$ | Rotor solidity, $N_b$c / ($\pi$R), $[-]$ |

## INTRODUCTION

Low Reynolds number rotorcraft research has been reinvigorated following the recent success of the Martian helicopter, Ingenuity (Ref. 1). However, here on Earth, there has been a significant increase in low Reynolds number rotor research due to the ongoing development of novel rotorcraft concepts including electric Vertical Take-off and Landing (eVTOL) vehicles, Micro Air Vehicles (MAVs) and the continued demand for higher speed helicopters (Ref. 2).

Each of the mentioned research areas present differing challenges. MAVs have been shown to have reduced hovering efficiency due to increased profile drag of the blades and the development of a significant boundary layer (Ref. 3). Moreover, Ramasamy et al. (Ref. 4) performed a comprehensive experimental investigation using Particle Image Velocimetry

Presented at the Vertical Flight Society's 80th Annual Forum & Technology Display, Montréal, Québec, Canada, May 7–9, 2024.
Copyright © 2024 by the Vertical Flight Society. All rights reserved.

(PIV) to characterise the flow field of multiple blade geometries at a tip Reynolds number of 35,000. A single bladed rotor investigation conducted by Wild et al. (Ref. 5) at a hovering tip Reynolds number of 26,000 further investigated different blade geometries by studying the effect of blunt and sharp trailing edges on the aerodynamic loads. A four bladed investigation was also performed to identify and quantify vortex structures, showing a reduction in the reverse flow wake area, highlighting a delay in flow separation for a blunt trailing edge. (Ref. 6).

Larger scale reverse flow investigations have also been performed. Datta et al. (Ref. 7) tested a full scale UH-60A rotor at slowed RPM conditions to investigate blade aerodynamic and aeroelastic performance, developing a high resolution large Reynolds number database. Furthermore, a series of works by Lind et al. (Refs. 8–13) investigated the reverse flow region for both static and rotating aerofoil sections for Reynolds number ranges between $10^5 - 10^6$. Areas of study included blade trailing edge geometries, thicker aerofoil sections, flow field characterisation using 2D PIV, influence of shaft angle on the reverse flow dynamic stall vortex (RFDSV) and unsteady surface pressure measurements.

Even though a very good understanding of the negative implications that reverse flow has on rotor aerodynamic and aeroelastic performance (excessive unsteady loads leading to large blade vibrations), experimental investigations are typically limited when compared to the vast amount of analytical and numerical literature. It is clear that very limited experimental data exists for low Reynolds number conditions. Of the limited data, almost all of the data is focused on the flow topology and global blade loading, highlighting the lack of aeroelastic data for rotors at low Reynolds numbers.

Therefore, similar to the recent investigation by Croke et al. (Ref. 14) investigating tilt-rotor blade structural response using strain gauges (Reynolds numbers approximately $10^5 - 10^6$), an investigation of blade structural response at low Reynolds number conditions will be undertaken. Load data will be measured to characterise the rotor aerodynamic environment for a range of advance ratios, in addition to multiple measurements of blade strain across the span to characterise the blade structural behaviour. This investigation will aim to form a comprehensive aeroelastic dataset of a single rotor blade at low Reynolds conditions.

## EXPERIMENTAL SETUP

An experimental investigation was undertaken at the Separated and Transient Aerodynamics Laboratory (STAL) at the University of Maryland to assess both the aerodynamic performance and aeroelastic behaviour of a fixed collective rotor blade in both hovering and edgewise flight at low Reynolds number conditions for large advance ratios.

### TOWING TANK AND ROTOR RIG

Testing was performed in the free surface water towing tank facility, where the tank dimensions are 1.5m x 1m x 7m (Width x Height x Length). The rotor rig was situated on the centre line of the towing tank to reduce rotor-wall interactions (blockage effects). As shown in the schematic of the experimental setup, presented in Figure 1, the blade is mounted onto the rotor hub which is connected to two control rods which are driven by a motor located on the tow carriage to provide rotational motion of the blade. The tow carriage is driven by a separate motor to provide a translation movement of the blade within the tank. The rig design allows for the blade collective to be easily varied between tests by swapping collective adapters. A full description of the rotor rig setup can be found in (Ref. 5).

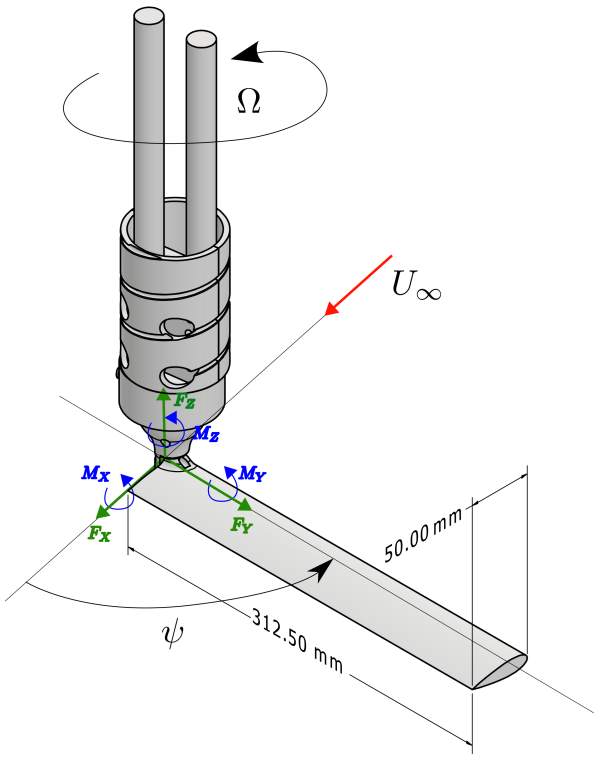


**Figure 1. Experimental setup used to perform rotor testing within the towing tank at the University of Maryland. Blade axes, rotational direction and freestream velocity directions are all specified.**

Moreover, the rotor rig allows for load data from the rotor blade such as thrust (T) and torque (Q) to be measured using the ATI six degree-of-freedom (6-DOF) Mini-40 IP68 force/torque sensor. Load data obtained by the load cell was corrected by means of a moment transfer to account for the offset in the vertical displacement of the load cell measuring surface and the blade quarter chord. Load data was acquired at a sampling rate of 1 kHz and synchronised with the towing tank motor encoders. Sampling periods were dependant on rotor advance ratio, ranging from approximately 15 to 240 seconds per run. To ensure repeatability and accuracy of the experimental data logged, five runs were performed for each advance ratio per collective.

## BLADE DESIGN AND INSTRUMENTATION

Testing of a single constant chord rotor blade of 0.3125m radius (R) and 0.05m chord (c) was undertaken. The blade design incorporates a NACA 0024 profile across the entirety of the span. This profile was chosen for two reasons:

1. Allows for the installation of wired strain gauges into the internal sections of the blade, ensuring no influence on the flow behaviour on the blade surface.
2. The NACA 0024 series aerofoil is a very well understood aerofoil with an abundance of experimental data across a range of Reynolds numbers.

Moreover, the blade was manufactured at the University of Maryland using a precision 3D printer. During the manufacture of both the upper and lower blade skins, carbon fibre composite layers were included to strengthen the blade and act as a blade spar, thus making the tested blade representative internally of a conventional rotor blade design. Sufficient internal spacing was left for the installation of blade instrumentation, wiring and waterproofing material prior to bonding. A summary of blade features and fluid properties is shown in Table 1.

**Table 1. Main features of the rotor blade and experimental setup.**

| Characteristic | Symbol | Value |
|---|---|---|
| Aerodynamic profile | - | NACA 0024 |
| Aspect ratio | - | 6.25 |
| Taper | - | Non-tapered |
| Twist distribution | - | Non-twisted |
| Radius | $R$ | 0.3125 $m$ |
| Diameter | $D$ | 0.625 $m$ |
| Chord | $c$ | 0.05 $m$ |
| Number of blades | $N_b$ | 1 |
| Solidity | $\sigma$ | 0.051 |
| Disk area | A | 0.3067 $m^2$ |
| Collective | $\theta$ | $7^o$ / $25^o$ |
| Kinematic viscosity | $\nu$ | $1.004 \times 10^{-6}$ $m^2/s$ |
| Fluid density | $\rho$ | 998 $kg/m^3$ |

The rotor blade has been instrumented with fully bridged axial strain gauges, totalling 3 bridges across the blade. The bridges have been arranged to measure the flap bending (FB) of the blade and are located at the following radial locations (y/R) 0.25, 0.5 and 0.75 as shown in Figure 2. Two gauges are co-located on the upper blade surface and two on the lower, at the same radial location. This full-bridge arrangement compensates for centrifugal loading and thermal deformation, so that the bridge reading $\varepsilon_B$ is representative of the difference in flap bending strain between the upper and lower surface of the blade. Measurements of local bending are transmitted from the rotating frame to the stationary frame via the Parker-Lord V-Link-200 telemetry system from which strain time histories were sampled at a frequency of 1024 Hz.

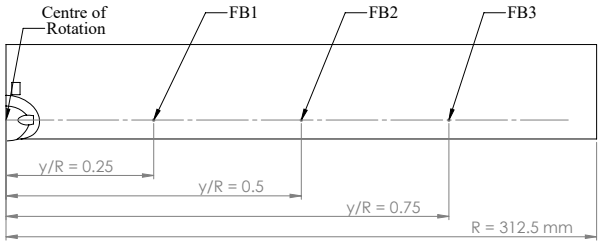


**Figure 2. Span wise location of flap-bending (FB) strain gauge bridges on the instrumented blade.**

# TEST MATRIX

Tests were conducted at both hover and advance flight, at advance ratios ($\mu$) ranging between 0.40 and 1.00 for two collective angles ($\theta$) of $7^o$ and $25^o$. The $7^o$ case will be used to investigate the blade response in attached flow on the advancing side of the rotor, whereas the $25^o$ case will be used to study the blade response in separated flow conditions around the entire azimuth.

## HOVERING FLIGHT

Hover testing was completed at three different rotational speeds of 16, 20 and 24 RPM. Load data and strains were captured to evaluate the impact of rotational speed on blade structural response at hover. Similar to Hein and Chopra (Ref. 3), a small study into rotor hover efficiency was performed. This will act as a benchmark from which blade response in forward flight can be compared against. Testing at hover was performed for both collective angles of $7^o$ and $25^o$.

## ADVANCE FLIGHT

Testing was performed at five high advance ratio conditions, ranging from $\mu = 0.40$ to 1.00 in equally spaced increments of 0.15. A constant rotor rotational speed of 20 RPM was selected due to the load limitations of the force balance. The rotor tip speed ($V_{TIP}$) was $0.655 m/s$ with a corresponding tip Reynolds number ($Re_{TIP}$) of $32,600$. Also, higher rotational speeds result in larger tip speeds, therefore any increase above 20 RPM for this blade would have limited the maximum available advance ratio due to translation motion speed limitation of the towing tank. The corresponding speeds and Reynolds number at each advance ratio are shown in Table 2.

# RESULTS

## HOVERING FLIGHT

To establish a series of baseline data that can be used to compare to the rotor performance in forward flight, both coefficients of rotor thrust and torque were determined at hovering conditions. Three rotational frequencies of 16, 20 and 24 RPM were studied to assess the dependency of the measurements on Reynolds number.

**Table 2. Test matrix of advance conditions showing advance ratio, forward tow velocity and Reynolds number.**

| Advance Ratio $\mu$ (-) | Tow Velocity $U_\infty$ $(m/s)$ | Reynolds Number $Re$ (-) |
|---|---|---|
| 0.40 | 0.26 | 13,000 |
| 0.55 | 0.36 | 17,900 |
| 0.70 | 0.46 | 22,800 |
| 0.85 | 0.56 | 27,700 |
| 1.00 | 0.65 | 32,600 |

Rotor thrust coefficients were shown to be effectively independent of RPM variation and were quantified at $C_T = 0.0017$ and 0.0057 for $\theta = 7^o$ and $\theta = 25^o$ respectively, for a rotational frequency equal to 20 RPM. The increase in thrust can be attributed to the increased rotor collective angle.

Measurements of rotor torque coefficient were found to be $C_Q = 0.00039$ and 0.0024 for $\theta = 7^o$ and $\theta = 25^o$, respectively for a rotational frequency equal to 20 RPM. Torque measurements were shown to drastically increase for the $\theta = 25^o$ case due to the nature of the stalled flow increasing both the active and passive torque. Moreover, torque measurements were also found to be slightly dependant on Reynolds number, with increasing RPM. Again, this can be attributed to the presence of stall around the entire rotor azimuth.

An assessment of rotor hovering efficiency was undertaken by evaluating both disc loading and Figure of Merit (FoM) parameters for a rotational frequency equal to 20 RPM. Disc loading was evaluated to be 0.72 and 2.45 for $\theta = 7^o$ and $\theta = 25^o$, respectively. Rotor FoM values for both collective angles were found to be 0.124 and 0.133, respectively.

Firstly, FoM results shown here must be interpreted with some degree of scepticism as the rotor disc loading for which they have been evaluated for is not constant. This means due to the increase in thrust, the induced component of the power has risen relative to the profile component of power. Nonetheless, FoM results can still be used individually to provide an insight into the rotor hovering efficiency. For both collective settings, a very low FoM was obtained. This can be explained by the chosen blade design, which incorporates a NACA 0024 aerofoil section (max thickness of 24%) across the entirety of the span, leading to an increase in profile drag due to thicker aerofoil section than that of the commonly used NACA 0012. Moreover, the blade is not an optimised geometry, as it does not include a taper or twist distribution along the span. Furthermore, the blade tip does not make use of a rounded edge and is abruptly ended, leading to increased tip losses.

However, despite the non-optimised geometry (required for the installation of strain gauges at such a small scale), the blade design is used to investigate unconventional and simplified rotor geometries that are likely to be incorporated in drones, small Unmanned Air Vehicle (UAVs) and MAVs. Typically, for rotor of this size, high-fidelity blade design is not feasible unless for military applications.

## ADVANCE FLIGHT

Before analysis of rotor strain behaviour can be fully appreciated, insight of the rotor aerodynamic environment in question can be very useful. To provide some insight into this environment, rotor blade performance is evaluated using coefficients of both thrust and torque. Analysis of the data in coefficient form allows for meaningful quantification of blade performance, as blade performance can be directly compared to that of other rotor blades of various scales and design parameters. Therefore, to adequately characterise the blade in forward flight, rotor loading and torque demand as a function of azimuthal position are presented in Figure 3.

Figures 3(a) and 3(c) show rotor thrust coefficient at $\theta = 7^o$ and $\theta = 25^o$, respectively. For both collective angles, thrust measurements display the same trend of behaviour despite the $\theta = 25^o$ case being stalled around the entirety of the azimuth, due to an excessive angle of attack. Firstly, focusing on the advancing side of the rotor disc ($0^o < \psi < 180^o$), as expected, the reduced collective angle results in lower measurements of peak thrust for a given advance ratio when compared to the $\theta = 25^o$ case. It is also observed for both collectives tested, that as the advance ratio is increased, the magnitude of the thrust also increases. Despite the similarities in the behaviour of the thrust data for both collectives, there is a noticable difference in the azimuthal position at which the peak loading occurs. For $\theta = 7^o$ peak loading occurs at approximately $\psi = 90^o$ whereas at $\theta = 25^o$ peak loading occurs at approximately $\psi = 75^o$.

Shifting the focus to the retreating side of the rotor disc ($180^o < \psi < 360^o$), it can be observed for both collective angles that there in a minima of rotor loading at approximately $\psi = 250^o$. Due to the large advance ratios that were tested, the blade in the retreating section of the disc is subjected to increased reverse flow effects for $\mu > 0.4$. This can be appreciated clearly from the negative thrust measurements, meaning the blade is thrusting in the opposing direction from the advancing side of the rotor disc. Moreover, for increasing advance ratios the magnitude of the negative thrust grows due to the increased region of the blade surface area that is subjected to the reverse flow. For example, at an advance ratio of 1, the entire blade is entrained in reversing flow when at $\psi = 270^o$ on the retreating side of the rotor disc.

Similar to the thrust behaviour, measurements of blade torque (shown in Figures 3(b) and 3(d)) detail the required rotor power for both collective angles. For the $\theta = 25^o$ case, there is a significant torque increase with respect to the $\theta = 7^o$ case.

$$C_P = \underbrace{\frac{kC_T^2}{2\mu}}_{\text{Induced Power}} + \underbrace{\frac{\sigma C_{d_0}}{8}(1+4.6\mu^2)}_{\text{Profile Power}} + \underbrace{\frac{C_D\mu^3}{2A}}_{\text{Parasitic Power}} \tag{1}$$

This can be explained by analysing the contributions of each of the power components as shown in Equation 1. An increase in induced power is a consequence of the large increase in blade thrust as a result of an increased collective. Profile

power increases due to the growth in advance ratio and parasitic power is increased due to the presence of stalled flow. Flow separation results in a large increase in blade drag which stems from the development of a separated region trailing the blade. Thus when all components are considered, the significant growth in rotor torque is appreciable.

To further quantify the rotor aerodynamic environment, Figure 4 presents mean rotor thrust and torque coefficient measurements for both collective settings as a function of advance ratio. In addition, the standard deviation of the measurements have been plotted as error bars to highlight the behaviour of the loading oscillations. The $\theta = 25^o$ case clearly demonstrates larger mean thrust and torque loads at all advance ratios when compared to the $\theta = 7^o$ case. It can also be observed that for both collectives, the thrust coefficient remains relatively constant with increasing advance ratio. However, when analysing the torque coefficient, it is clear for both collective angles, there is a growth in mean torque with advance ratio. This can be attributed to the fact that the growth in advance ratio increases the profile and parasitic drag of the rotor. Moreover, this increase is more apparent for the $\theta = 25^o$ case due to the presence of stalled flow. Finally, with regards to rotor loads, both collectives indicate a growth in thrust and torque oscillations as a consequence of increasing advance ratio. Again, the $\theta = 25^o$ case exhibits very large oscillations with respect to the $\theta = 7^o$ case, due to the presence of stalled flow and increased rotor loading.

Now that the rotor aerodynamic environment has been described and quantified, measurements of rotor strain can be presented. Measurements of rotor strain as a function of azimuthal position, for a range of advance ratios at two different radial locations, are presented in Figure 5.

Figures 5(a) and 5(c) show for the $\theta = 7^o$ case, measurements of rotor blade strain from FB1 and FB2 bridges to highlight the strain distribution along the blade span. It is apparent that the strain behaviour across both bridges on the advancing side of the rotor disc follows the behaviour exhibited by the thrust. For both FB1 and FB2 bridges, the peak strain occurs at approximately $\psi = 90^o$, identical to the peak loading shown in the thrust data. In addition, also just like the thrust data, an increase in advance ratio leads to a growth in peak strain magnitude. On the retreating side, the minima of strain appears to also align with the behaviour shown in the thrust data, with the strain minima occurring at approximately $\psi = 250^o$ for both FB1 and FB2. Focusing on FB1, it is clear for $\mu > 0.4$ there is an occurrence of negative strain on the retreating side of the disc, coinciding with the thrust minima location. Negative strain, indicates that the blade is being loaded in the opposing direction from the thrust axis, which is further indication of strong reverse flow effects. As the blade is non-twisted and non-tapered, the variation of strain magnitude across different bridges is useful to provide insight into loading distribution across the blade. However, it is important to note that the strain, although very dependant on loading, is not to be confused with a measure of loads, as the blade strain is also dependant on structural properties such as torsional and bending stiffness. Therefore, when comparing FB1 to FB2, it is clear that FB1 has a larger magnitude of strain at any azimuthal location. This is to be expected as the blade is secured to the rotor hub at the root, ensuring a fixed collective angle with no longitudinal or lateral cyclic. Therefore, in terms of strain distribution, the blade is representative of a cantilever beam and the strain would be expected to drop further outboard towards the tip.

Figures 5(b) and 5(d) show for the $\theta = 25^o$ case, measurements of rotor blade strain from FB1 and FB2 bridges. Identical to the $\theta = 7^o$ case, locations of maximum and minimum strain plus the behaviour of strain variation across the blade span at different bridge locations remains the same. However, due to the presence of stalled flow around the entire rotor azimuth, there is an unsteadiness in the strain measurement that can be visibly acknowledged (particularly in Figure 5(d)) by the variation in the smoothness of the strain on the advancing side of the rotor disc.

Similar to analysis of the load data, Figure 6 presents mean rotor strain measurements of individual bridges for both collective settings as a function of advance ratio. In addition, the standard deviation of the measurements have been plotted as error bars to highlight the behaviour of bridge strain unsteadiness. It is clear for the $\theta = 25^o$ case that the mean strain of any bridge is larger than that of the $\theta = 7^o$ case. This behaviour will primarily be a consequence of larger thrust loads. However, the presence of stalled flow will also have an influence on measured strain due to the large increase in rotor drag. Moreover, structural parameters such as stiffness will also influence the measured strain.

To visualise the strain distribution across the blade more clearly, Figure 7 presents mean rotor strain measurements for different bridges for a given collective. As previously mentioned, it is clear that closer to the blade root there is a growth in mean strain and a reduction towards the blade tip. For both collective angles, the oscillation in the measured strain at FB1 is significantly large due to the location of the bridge on the blade, as the most inboard bridge at 25% of the blade span this bridge is subjected to reverse flow at the lower advance ratios tested.

Finally, to further highlight the presence of stalled flow. Figure 8 presents the spectral content of FB1 at advance ratios of 0.4 and 1.00 for both collective angles. The spectra is shown as the non-dimensional frequency to highlight the dominant 1/rev signal and the surrounding broadband of the signal. It is clear from the $\theta = 7^o$ case shown in Figure 8(a) that there is very limited broadband content within the signal and is dominated by a single rotor harmonic (1/rev). In contrast, the $\theta = 25^o$ case shows a large distribution of signal energy across a range of non-harmonic frequencies. This can be explained by the stalled flow resulting in aperiodic vortex shedding as the vorticity shed into the wake will likely not occur synchronously with that of the rotor harmonics. Figure 8(b) further confirms this behaviour as the $\theta = 25^o$ case continues to display a large distribution of signal energy across a range of non-harmonic frequencies. Moreover, as expected, the magnitude of signal energy is larger for the $\theta = 25^o$ case.

## CONCLUSIONS

A towing tank investigation of a single rotor blade operating at hovering and high advance ratio conditions has been presented. A custom blade was manufactured and instrumented with fully bridged axial strain gauges to monitor the flap bending strain at three radial locations. Measurements of rotor thrust and torque to characterise the rotor aerodynamic environment were acquired using a 6-DOF load cell. The rotor was tested in both hovering and advancing flight for advance ratios ranging between 0.4 to 1.00 at two fixed collective angles of $\theta = 7^o$ and $25^o$.

1. During hover, thrust measurements were found to be independent of the influence of Reynolds number whereas the torque was shown to be somewhat dependant. For $\theta = 25^o$, both thrust and torque measurements we shown to increase with respect to $\theta = 7^o$. Moreover, the non-optimised blade design showed relatively poor values of FoM for both collective settings.

2. A characterisation of the rotor aerodynamic environment for cases of advance flight at high advance ratios was undertaken. Thrust and torque measurements obtained identified regions of reverse flow at approximately $\psi = 250^o$ for both collective angles where $\mu > 0.4$.

3. Strain measurements obtained at three locations across the blade span show identical minima and maxima locations on the azimuth to the load data. The strain distribution shows a growth in strain magnitude with increasing advance ratio. Moreover, for a given advance ratio, strain is highest towards the root and decreases towards the blade tip.

4. Spectra results of the strain show that a dominant 1/rev signal can be clearly identified for both collective angles. For the $\theta = 25^o$ case, a large distribution of signal energy across a range of non-harmonic frequencies is observed due to aperiodic vortex shedding from the presence of stalled flow.

This investigation serves as a baseline for future experimental testing to further understand the aerodynamic and aeroelastic behaviour of rotors operating at low Reynolds number conditions in both hovering and edgewise flight.

Author contact:

| | |
|---|---|
| Alexander Croke | a.croke.1@research.gla.ac.uk |
| Oliver Wild | owild@umd.edu |
| Anya Jones | arjones@umd.edu |
| Richard Green | richard.green@glasgow.ac.uk |


## ACKNOWLEDGEMENTS

The authors would like to acknowledge the assistance of Dr Daniele Zagaglia (University of Glasgow) and Antonios Gementzopoulos (University of Maryland).

Alexander D. Croke would like to acknowledge the financial support from the University of Glasgow post graduate research travel fund and the University of Glasgow college of science and engineering global mobility scholarship 2023.

This work was funded by The United States National Science Foundation award number 2247006.

## REFERENCES

1. W.J.F. Koning, B.G. Allan, E.A. Romander, and W. Johnson. Comparing 3d and 2d cfd for mars helicopter ingenuity rotor performance prediction. In *49th European Rotorcraft Forum, Buckeburg, Germany*, 05-07 Sep 2023.

2. Graham Bowen-Davies and Inderjit Chopra. Investigation of the unsteady reverse flow airloads at high advance ratios. In *41st European Rotorcraft Forum, Munich, Germany*, 01-04 Sep 2015.

3. Benjamin R Hein and Inderjit Chopra. Hover performance of a micro air vehicle: rotors at low reynolds number. *Journal of the American Helicopter Society*, 52(3):254–262, 2007.

4. Manikandan Ramasamy, Bradley Johnson, and J Gordon Leishman. Understanding the aerodynamic efficiency of a hovering micro-rotor. *Journal of the American Helicopter Society*, 53(4):412–428, 2008.

5. Oliver Wild, Matthew J Murphy, and Anya R Jones. Comparison of instantaneous aerodynamic loads on sharp and blunt trailing-edged blades of high advance ratio rotors. In *AIAA SciTech 2023 Forum*, page 2466, 2023.

6. Oliver D Wild and Anya R Jones. Vortex identification and quantification on blunt trailing-edge rotor blades in reverse flow. *AIAA Journal*, pages 1–16, 2023.

7. Anubhav Datta, Hyeonsoo Yeo, and Thomas R Norman. Experimental investigation and fundamental understanding of a full-scale slowed rotor at high advance ratios. *Journal of the American Helicopter Society*, 58(2):1–17, 2013.

8. Andrew H Lind, Lauren N Trollinger, Field H Manar, Inderjit Chopra, and Anya R Jones. Flowfield measurements of reverse flow on a high advance ratio rotor. *Experiments in Fluids*, 59:1–15, 2018.

9. Andrew H Lind, Luke R Smith, Joseph I Milluzzo, and Anya R Jones. Reynolds number effects on rotor blade sections in reverse flow. *Journal of Aircraft*, 53(5):1248–1260, 2016.

10. Andrew H Lind, Jonathan N Lefebvre, and Anya R Jones. Time-averaged aerodynamics of sharp and blunt trailing-edge static airfoils in reverse flow. *AIAA journal*, 52(12):2751–2764, 2014.

11. Andrew H Lind and Anya R Jones. Unsteady aerodynamics of reverse flow dynamic stall on an oscillating blade section. *Physics of Fluids*, 28(7), 2016.

12. Andrew H Lind and Anya R Jones. Unsteady airloads on static airfoils through high angles of attack and in reverse flow. *Journal of Fluids and Structures*, 63:259–279, 2016.

13. Andrew H Lind and Anya R Jones. Vortex shedding from airfoils in reverse flow. *AIAA Journal*, 53(9):2621–2633, 2015.

14. Alexander D. Croke, Daniele Zagaglia, Mark A. Woodgate, Richard B. Green, and George N. Barakos. Experimental investigation into the onset of stall flutter on tiltrotor blades. In *49th European Rotorcraft Forum, Buckeburg, Germany*, 05-07 Sep 2023.

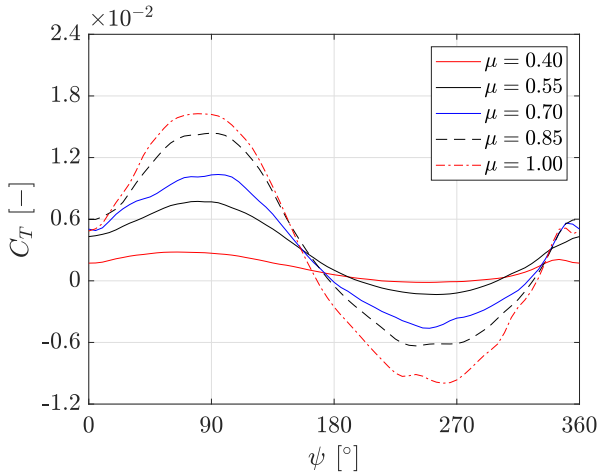


(a) $C_T$ at $\theta = 7°$

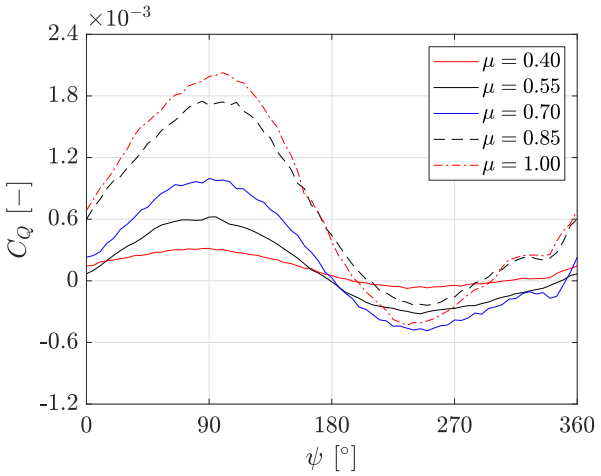


(b) $C_Q$ at $\theta = 7°$

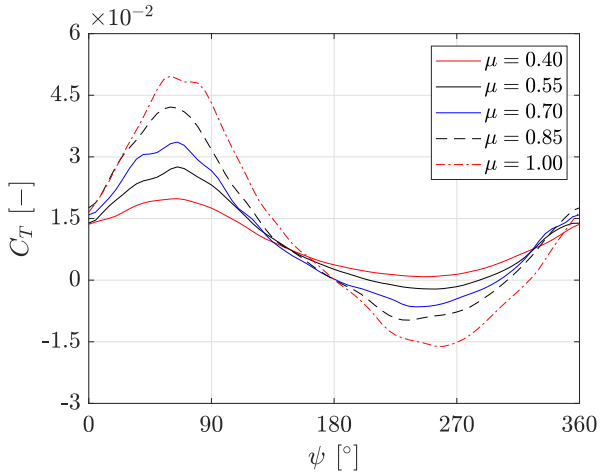


(c) $C_T$ at $\theta = 25°$

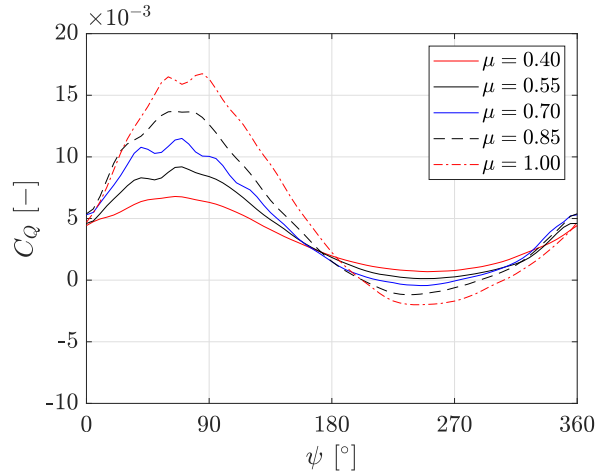


(d) $C_Q$ at $\theta = 25°$

**Figure 3. Coefficients of thrust ($C_T$) and torque ($C_Q$) of a rotor blade in advance flight ($\mu = 0.40 - 1.00$) at a collective angles of $\theta = 7°$ and $25°$ shown as a function of rotor blade azimuthal position ($\psi$).**

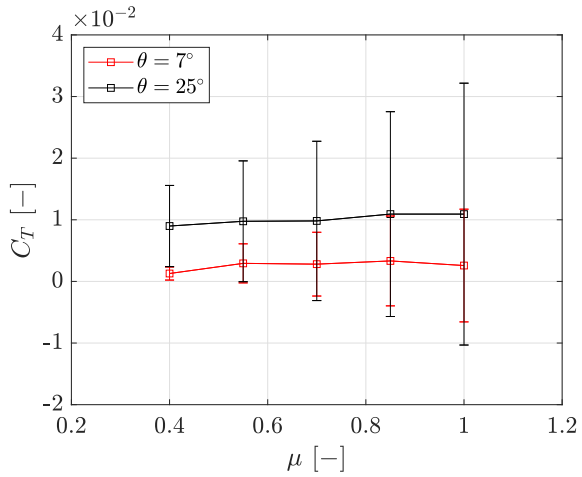


(a) $C_T$

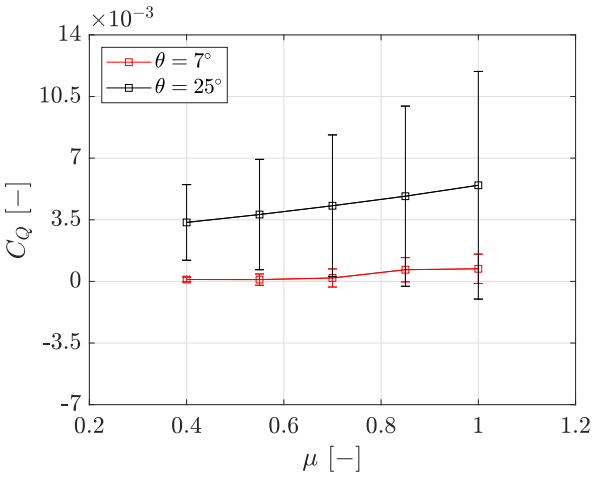


(b) $C_Q$

**Figure 4. Mean coefficients of thrust ($C_T$) and torque ($C_Q$) measurements for both collective settings as a function of advance ratio. Error bars added to show the standard deviation of the measurements.**

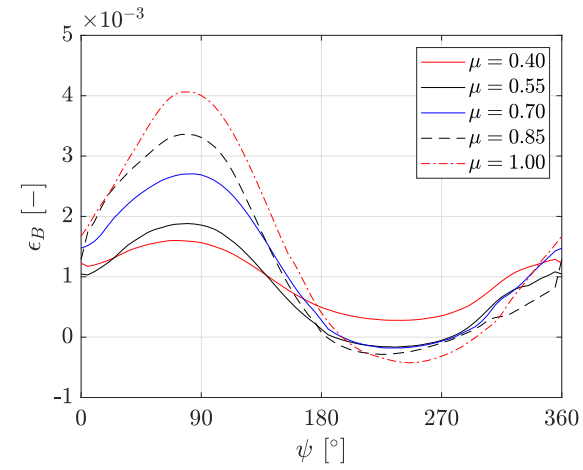


(a) FB1 at $\theta = 7°$

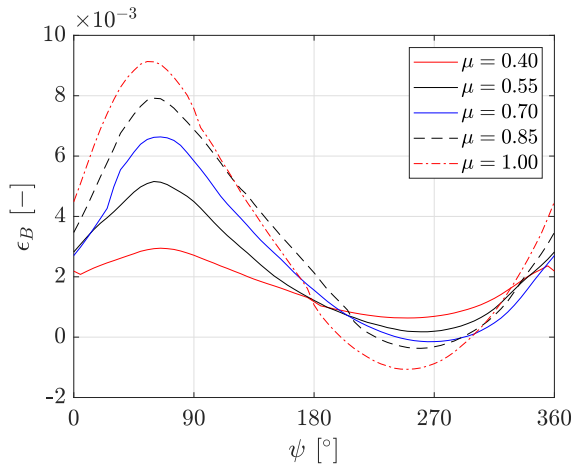


(b) FB1 at $\theta = 25°$

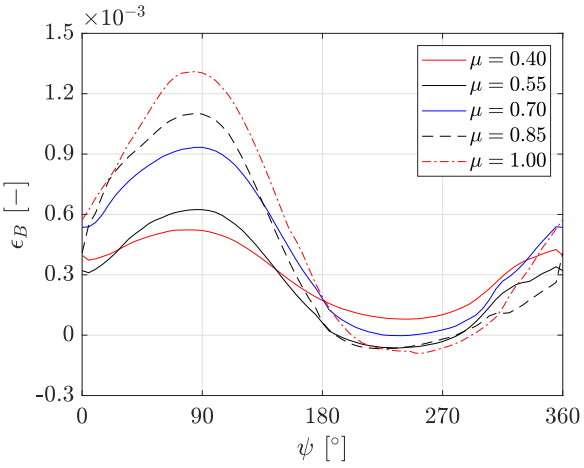


(c) FB2 at $\theta = 7°$

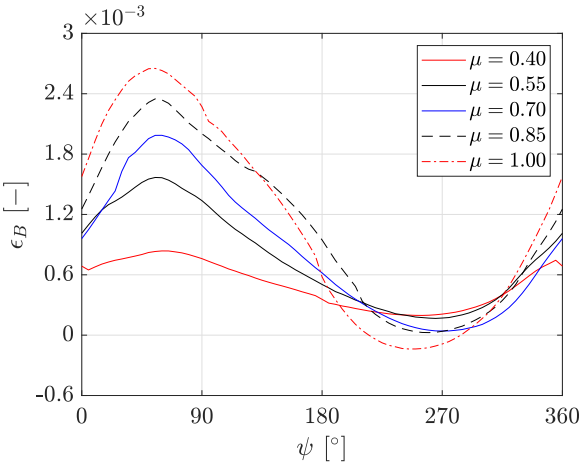


(d) FB2 at $\theta = 25°$

**Figure 5. Strain ($\varepsilon_B$) at FB1 ($y/R = 0.25$) and FB2 ($y/R = 0.50$) in advance flight ($\mu = 0.40 - 1.00$) at collective angles of $\theta = 7°$ and $\theta = 25°$ shown as a function of rotor blade azimuthal position ($\psi$).**

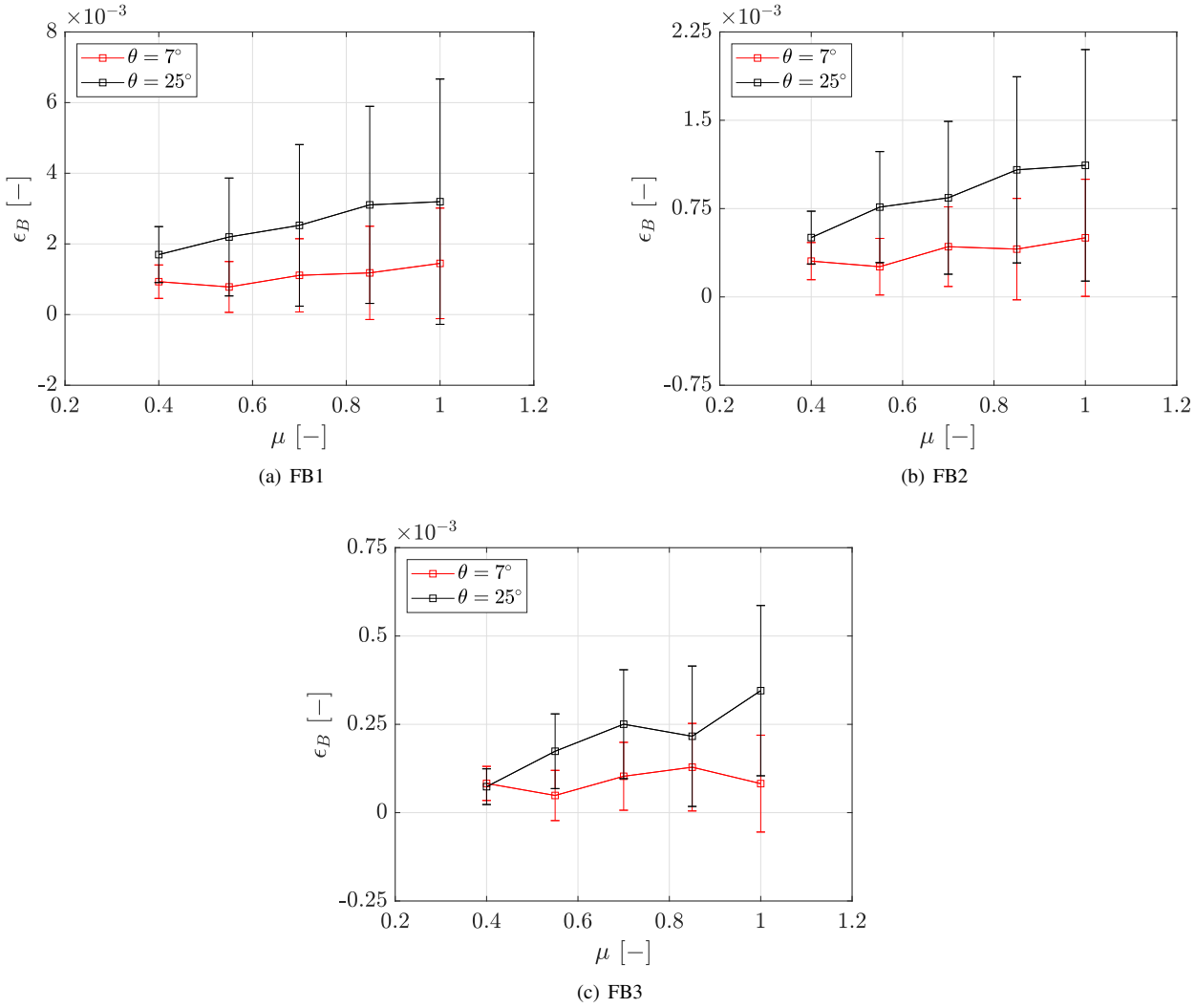


(a) FB1

(b) FB2

(c) FB3

**Figure 6. Mean strain ($\varepsilon_B$) measurements for both collective settings as a function of advance ratio for individual bridges FB1, FB2 and FB3. Error bars added to show the standard deviation of the measurements.**

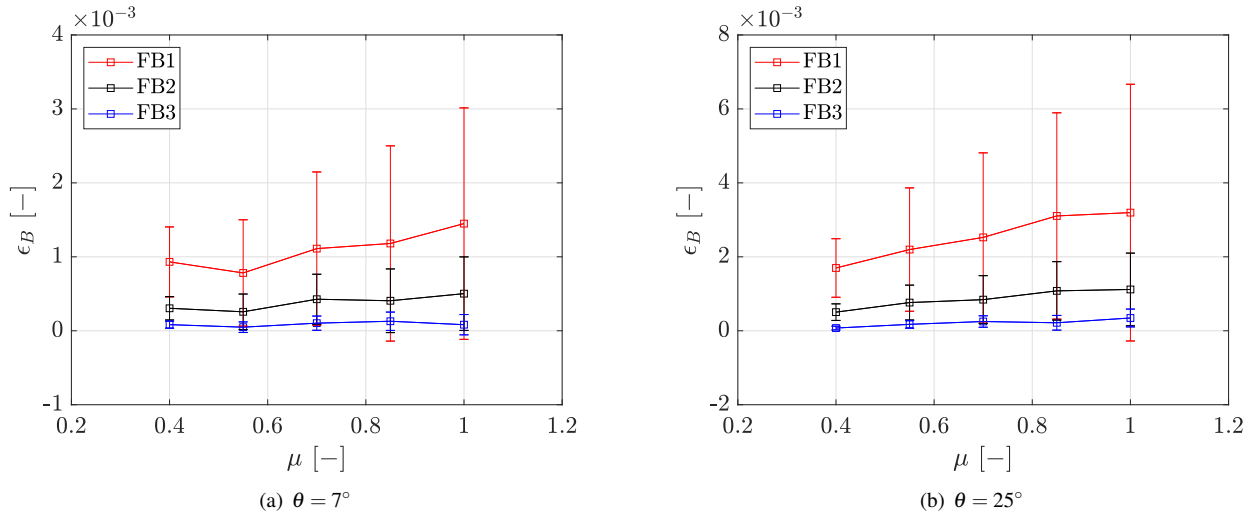


(a) $\theta = 7°$

(b) $\theta = 25°$

**Figure 7. Mean strain ($\varepsilon_B$) measurements for a given collective setting as a function of advance ratio presenting the strain distribution of FB1, FB2 and FB3. Error bars added to show the standard deviation of the measurements.**

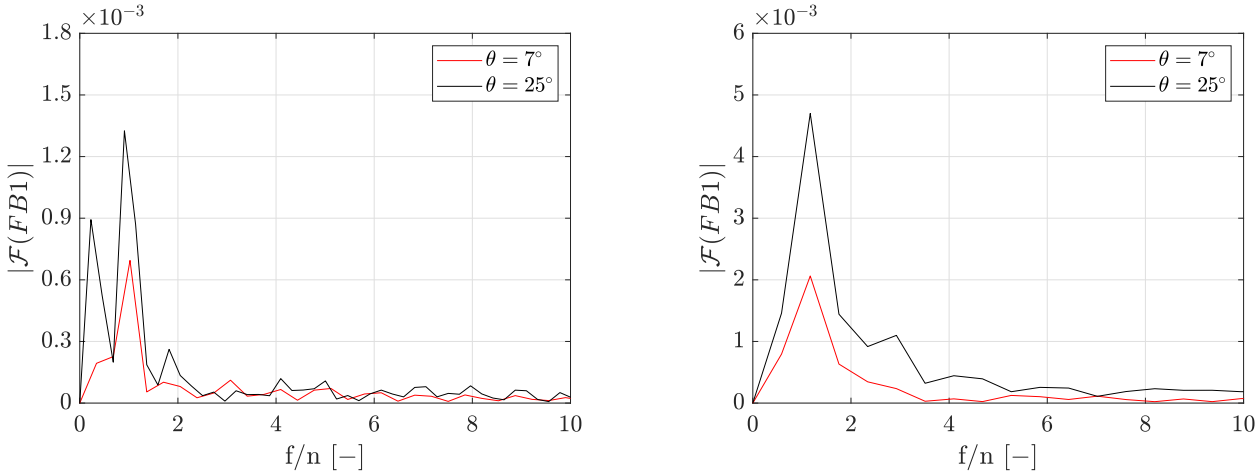


(a) $\mu = 0.4$ (b) $\mu = 1.00$

**Figure 8. Amplitude of the Fourier transform (as a function of the non dimensional frequency f /n) of the strain measurements for FB1 at $\theta = 7°$ and $\theta = 25°$ for advance ratios of 0.4 and 1.00.**